Effects of pore collapse and grain crushing on ultrasonic velocities and Vp/Vs

Jérôme Fortin, Yves Guéguen, Alexandre Schubnel

Effects of pore collapse and grain crushing on ultrasonic velocities and V_p/V_s

Jérôme Fortin,[1] Yves Guéguen,[1] and Alexandre Schubnel[2]

Received 20 August 2005; revised 13 February 2007; accepted 6 June 2007; published 21 August 2007.

[1] Compressional, shear wave velocities and their ratio, V_p/V_s, were measured along with porosity variations during wet and dry hydrostatic compaction of Bleurswiller sandstone, a 25% porosity Vosgian sandstone. At first, increase in hydrostatic pressure was accompanied by a simultaneous increase of both V_p and V_s as expected. At a critical effective confining pressure P^*, a large mechanical decrease of porosity was observed that was due to pore collapse and grain crushing. Theoretically, two different processes are affecting the elastic wave velocities in counteracting ways during cataclastic compaction: cracking and porosity decrease. Our experimental results show that cracking is the dominant effect, so that grain crushing and porosity reduction were accompanied by a large decrease in velocities. The ratio V_p/V_s was also observed to change during our experiments: In the wet specimen, V_p/V_s value increased from 1.72 to 1.84, while in the dry specimen, it increased from 1.59 below P^* to 1.67 beyond P^*, respectively. To quantitatively interpret these results, an isotropic effective medium model (EM) was used that considered the sandstone as a mixture of spheroidal pores and penny-shaped cracks. In particular, the increase in V_p/V_s, in the wet case, is well reproduced and shows the important role played by the mechanical coupling of fluid with low aspect ratio cracks ($<10^{-2}$). In the dry case, however, our experimental results highlight an increase of V_p/V_s ratio during cataclastic compaction, in apparent contradiction with the predictions of the EM model. Indeed, increases in V_p/V_s ratio, and hence in Poisson's ratio, are, in general, attributed to fluid saturation. A closer look to the microstructure may provide a possible interpretation: Beyond P^*, grains are no longer cemented. Using Digby's granular model as an alternative model, we were able to reach a quantitative agreement with the experimental results. The possible implication is that in both dry and wet conditions, cataclastic compaction due to grain crushing induces an increase in V_p/V_s ratio.

Citation: Fortin, J., Y. Guéguen, and A. Schubnel (2007), Effects of pore collapse and grain crushing on ultrasonic velocities and V_p/V_s, *J. Geophys. Res.*, *112*, B08207, doi:10.1029/2005JB004005.

1. Introduction

[2] Compaction can occur as a result of mechanical and chemical processes [*Wong et al.*, 2004; *Lehner and Leroy*, 2004]. While chemical compaction usually becomes the dominant process at depths greater than 4.5 km [*Giles*, 1997; *Ramm*, 1992], mechanical compaction involves the rearrangement of grains at lower depths. Mechanical compaction and associated porosity reduction play an important role in the diagenesis of sandstones and they may also affect sandstone reservoirs during hydrocarbon production [*Smits et al.*, 1988; *Fredrich et al.*, 1998]. In such cases, mechanical compaction may occur because production decreases the pore pressure and hence increases the effective stress on the sandstone solid matrix. Results from hydrostatic compaction experiments on a wide range of sands and sandstones are generally interpreted in terms of a critical pressure P^*, which characterizes the onset of homogeneous pore collapse and grain crushing (nonlocalized cataclastic flow) [*Zhang et al.*, 1990; *Wong et al.*, 1997].

[3] Recent field [*Mollema and Antonellini*, 1996], and laboratory [*Olsson*, 1999; *Klein et al.*, 2001; *Baud et al.*, 2004; *Fortin et al.*, 2005, 2006] observations have focused attention on the formation of localized compaction bands in porous sandstones. Laboratory experiments have shown that compaction bands occurred in sandstones with porosities ranging from 20 to 28%, deformed at room temperature, under a triaxial loading. The present investigation is restricted to conditions of zero deviatoric stress (purely hydrostatic compaction) as the case of nonzero deviatoric stress in Bleurswiller sandstone has been previously reported by *Fortin et al.* [2005, 2006]. In such experimental conditions, compaction bands can theoretically not occur [*Rudnicki*, 2004], and the deformation is assumed to be homogeneous (principle of symmetry).

[4] The measurement of elastic wave velocities has often been used to provide some information about the rock

[1] Laboratoire de Géologie, Ecole Normale Supérieure, Paris, France.
[2] Lassonde Institute, University of Toronto, Toronto, Ontario, Canada.

0148-0227/07/2005JB004005$09.00

microstructure [e.g., *Nur and Wang*, 1989]. Being by nature small mechanical perturbations, elastic waves are strongly affected by the rock deformation processes. In consequence, the behavior of the elastic wave velocities (V_p and V_s, and their ratio V_p/V_s) during pore collapse and grain crushing is not straightforward. Indeed, elastic wave velocities can be affected by two distinct and competitive mechanisms: (1) cracking and (2) porosity reduction. In the first case, it is well known that elastic wave velocities may be reduced substantially during triaxial compression experiments in the presence of cracks. This is observed in crystalline rocks [e.g., *Hadley*, 1976], and also in porous rocks [e.g., *Scott et al.*, 1993]. Under hydrostatic tests, *Zhang et al.* [1990] and *Wong et al.* [1997] demonstrate from postmortem microstructural observations that grain crushing in sandstone is generally characterized by extensive microcracking as cracks nucleate and propagate when pressure reaches the critical pressure P^*. Therefore these newly formed cracks may induce a decrease in elastic wave velocities. Second, *Zhang et al.* [1990], *Wong et al.* [1997], and *Karner et al.* [2003] report for hydrostatic tests on porous sandstones, that pore collapse can induce a porosity reduction higher than 10%. Therefore porosity reduction may result in an increase of the elastic wave velocities [*Dvorkin and Nur*, 1996; *Avseth et al.*, 1998].

[5] Understanding the stress dependencies of seismic velocities is important for interpreting a variety of seismic data. The velocity dependence on confining pressure can be phenomenologically described [*Zimmerman et al.*, 1986; *Shapiro*, 2003] without specifying any micromechanical model. However, effective medium theories (EMT) connect the effective elastic properties of a rock to that of the solid matrix (pore- and crack-free), the fluid properties, and parameters related to pores and cracks such as the crack density ρ and the porosity p. Using EMT makes it possible to specify a macroscopic behavior relying on a microscopic mechanism. Two different approaches are frequently used in EMT calculations: (1) one is the approximation of an effective matrix and (2) the other is the approximation of an effective field. In the first case, each crack or pore is assumed to be isolated in a medium that is the effective matrix [*O'Connell and Budiansky*, 1974, 1977; *Salganik*, 1973; *Hashin*, 1988]. For example, using a differential self-consistent method, *Le Ravalec and Guéguen* [1996] calculated the effective elastic moduli of a two-phase material: an isotropic solid matrix containing an isotropic distribution of round pores or oblate spheroidal cracks. In the second case, crack interactions are accounted for through an effective stress. Of special interest is the model of noninteraction approximation. Indeed, using this assumption, the effective elastic properties of a material containing fluid-filled pores of various shapes can be calculated rigorously and exactly in a manner that depends on the crack and pore distributions solely [*Bristow*, 1960; *Walsh* 1965; *Kachanov*, 1980; *Sayers and Kachanov*, 1995]. The noninteraction assumption, often wrongly confused with the low crack density one, remains accurate at high crack densities, provided the locations of crack centers are random. Indeed, at a microscopic level, crack interactions exist but are approximately compensated. *Sayers and Kachanov* [1995] and *Schubnel and Guéguen* [2003] proved that this assumption is the best one for certain distributions such as random (isotropic) or aligned crack distributions. In such a way, the effective elastic moduli of a material containing a mixture of saturated pores and ellipsoidal cracks were given recently by *Shafiro and Kachanov* [1997]. In this model, the effective stress is estimated using the scheme of Mori-Tanaka (let us point out that if the material contains only cracks, the Mori-Tanaka scheme corresponds exactly to the noninteraction assumption).

[6] In this paper, we report experimental results obtained during the hydrostatic compaction of dry and saturated specimens of Bleurswiller sandstone (a Vosgian sandstone with an initial porosity $p = 25\%$). Elastic wave velocities (V_p and V_s, and their ratio V_p/V_s) were measured during these experiments: In the first parts of the loading, the application of the hydrostatic pressure closes the preexisting cracks and pores with low aspect ratios and raises the velocities. However, our data show that during pore collapse and grain crushing, elastic wave velocities decrease, which implies that they are more affected by cracks than by porosity reduction. To interpret theoretically and quantitatively these results, we consider a porous rock as made of a mixture of solid grains, spherical pores, and penny-shaped cracks. The effective medium model "pores and cracks" that we used here both in dry and fluid-saturated conditions, is based on the works of *Kachanov* [1993], *Kachanov et al.* [1994], and *Shafiro and Kachanov* [1997].

2. Experimental Methods

2.1. Sample

[7] Cylindrical specimens of 80 mm in length and 40 mm in diameter were prepared from Bleurswiller sandstone. This sandstone was collected from the quarry of Frain (Vosges, eastern France) and is identical to the one previously studied by *Fortin et al.* [2005, 2006]. Figure 1a gives a picture of an intact specimen. The physical properties are detailed in Table 1. Porosity is about 25%. *Fortin et al.* [2006] have investigated microstructure using optical microscopy: This gray sandstone contains ~50% quartz, ~30% feldspars, and ~20% oxides-micas and grain sizes range from 80 μm to 150 μm with a mean value of 110 μm. Figure 1b show a scanning electron microscopy (SEM) of an intact specimen, for comparison: Porosity appears in black, and quartz grains appear darker than the feldspar grains. Grains are mostly subangular to subrounded. Clay is often located within the pores, or between two grains. The microstructure analysis does not reveal any layering. Moreover, the undeformed sample has an initial P wave velocity anisotropy lower than 1.5%. We assume in the following that Bleurswiller sandstone is isotropic.

2.2. Laboratory Equipment

[8] The triaxial cell installed at the Laboratoire de Géologie of Ecole Normale Supérieure (Paris, France) was used to investigate the evolution of the elastic wave velocities in Bleurswiller sandstone deformed under hydrostatic loading. A schematic diagram of the apparatus is shown in Figure 2. The confining pressure is servo-controlled with an accuracy of 0.1 MPa and can reach 300 MPa. The confining medium is oil. The axial load can be achieved through an autocompensated hydraulic piston, but it was not used in the experiments presented in this study since we focus here

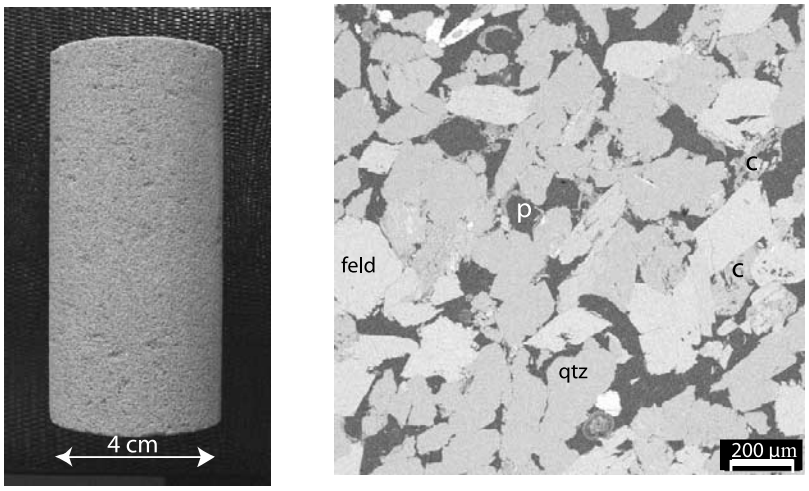

Figure 1. (a) Picture of a nondeformed sample of Bleurswiller sandstone. (b) SEM micrograph (backscattered) of an intact sandstone. Epoxy-filled pores (p) appear in black, porosity is about 25%. Quartz, feldspar, and clay are denoted by qtz, feld, and c, respectively.

on hydrostatic compaction with zero deviatoric stress. Pore pressure can be driven by two precision volumetric pumps. Pore fluid is introduced into the sample through hardened steel end pieces placed on the top and bottom of the rock sample. Maximum pore pressure in the system is 100 MPa. Both pumps can be controlled either in pressure (0.01 MPa precision), in flow (minimum flow is 0.1 $cm^3\ h^{-1}$) or in volume (precision approximately 0.005 cm^3). The main advantage of the triaxial apparatus is its 34 electric feedthroughs that can allow simultaneously measurements of ultrasonic *P* and *S* velocities, as well as local strains (strain gauges).

2.3. Strain Measurements

[9] The results of dry and wet experiments are presented in this study. In the dry experiment, volumetric stain ε_v was calculated from axial strain ε_z and radial strain ε_r using $\varepsilon_v = 2\varepsilon_r + \varepsilon_z$. Measurements were acquired using strain gauges (TML FLA-20, Tokyosokki) directly glued to sample's surface (Figure 3a). Each of strain gauge was mounted in a 1/4 Wheatstone bridge. Uncertainty in strain measurement was approximately 10^{-5}. Given that pores are much more compliant than solid grains, we assume that volumetric strain was equal to change in porosity.

[10] In the wet experiment, the sample was deformed under drained conditions at a constant pore pressure of 10 MPa. Pore pressure was maintained constant, and pore volume variation throughout the experiment was recorded using a volumometer, allowing a monitoring of the evolution of sample connected porosity. In this case, radial strain ε_r was determined using $\varepsilon_r = \varepsilon_v/3$.

2.4. Velocity Measurements

[11] Velocities are obtained using a pulse transmission method in which measured traveltimes of elastic wave through the rock and sample length, corrected from radial deformation, are used to calculate the velocities. *P* and *S* elastic wave velocities were measured perpendicular to axis–symmetric axis, along diameter of the sample (Figure 3a). To record *P* wave velocities we used source-receiver lead-zirconate piezoceramic discs (PZT) 10 mm in diameter and 1 mm in thickness (PI255, PI ceramics, resonant frequency of 1 MHz). Shear wave PZTs were plate $10 \times 10 \times 1$ in dimension. *P* and *S* wave PZTs were glued directly onto the sample surface and positioned with approximately 0.5 mm accuracy, while the distance between opposite (paired) PZTs from which the velocities were calculated was measured within 0.01 mm. The sending transducers are driven by a Dirac pulse, generated by a Sofranel® generator (approximately 370 V at 1 MHz frequency). The elastic wave produced by the first transducer is transmitted through the sample and detected by the second transducer. The resulting signals were recorded on an oscilloscope (Tektronix TDS-460A) and averaged over 50 waveforms. The oscilloscope digitized the averaged trace with 2500 points at a time sweep of 25 μs, thus allowing a time resolution of 10 ns. Then, the averaged signal is transferred to a laboratory computer for further processing. An example of received *S* waveforms, at different confining pressure is shown in Figure 3b. Traveltimes were determined using a double picking technique, i.e., the mean between (1) the first arrival and (2) the first peak of the signal, minus a quarter of period (Figure 3b). Traveltime calibration was accomplished by using aluminium rods of different lengths. In such conditions, the error in absolute

Table 1. Physical Properties of Bleurswiller Sandstone Used in This Study

Property	Value
Porosity	25%
Grain size, μm	80–180
Permeability, $\times 10^{-16}$ m^2	200
Initial *P* wave anisotropy, %	<1.5

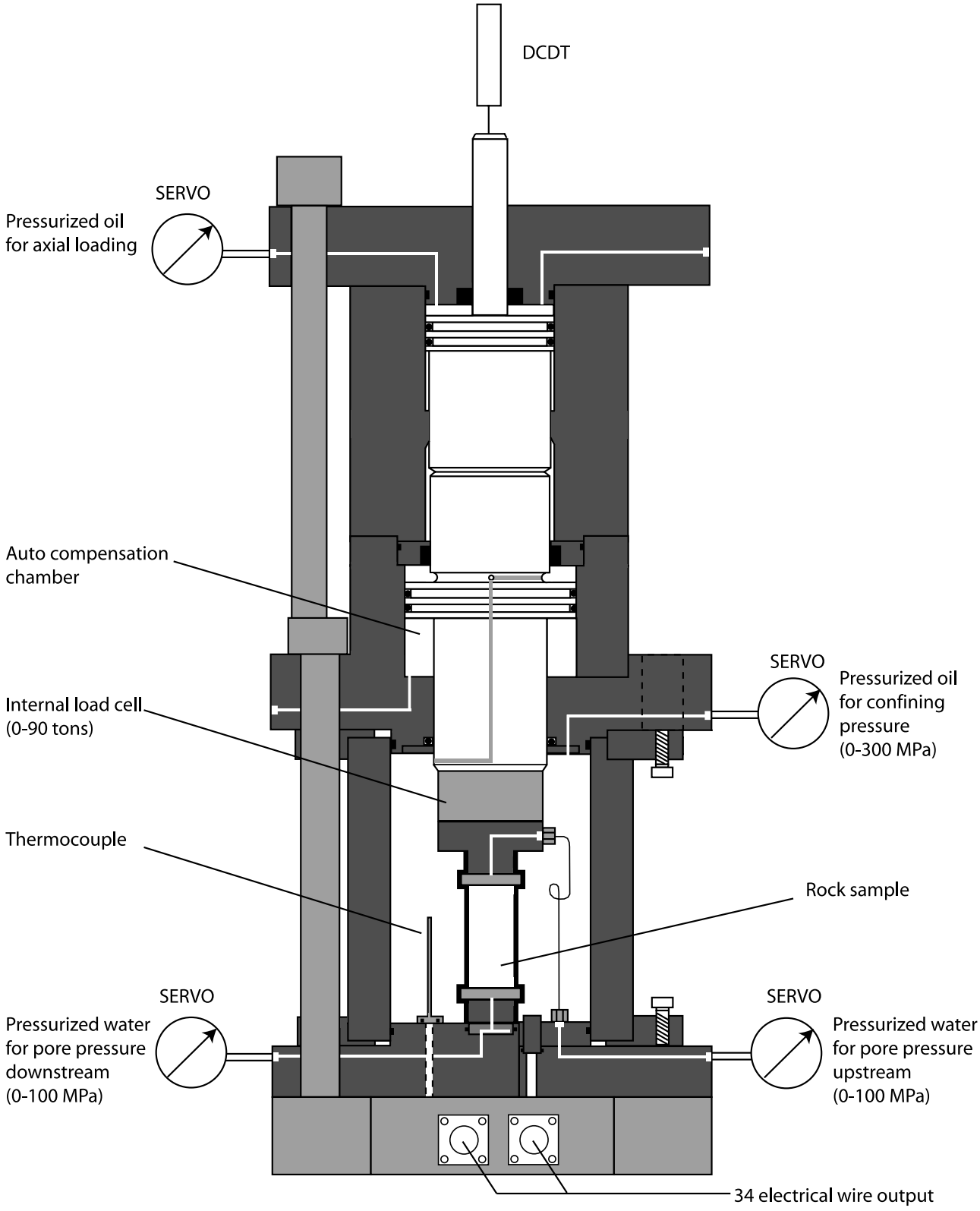

Figure 2. Schematic diagram of the triaxial high-pressure cell installed at the Laboratoire de Géologie of Ecole Normale Supérieure of Paris (France).

velocity is estimated to be less than 3%, but relative error between two consecutive measurements was reduced to 0.5%. Finally, *P* wave velocities (and *S* wave velocities) were determined using the average of values calculated along the two perpendicular trajectories (Figure 3a). In the same way, the ratio V_p/V_s was calculated as the average of the two ratios t_S/t_P (traveltimes), measured along the two perpendicular trajectories.

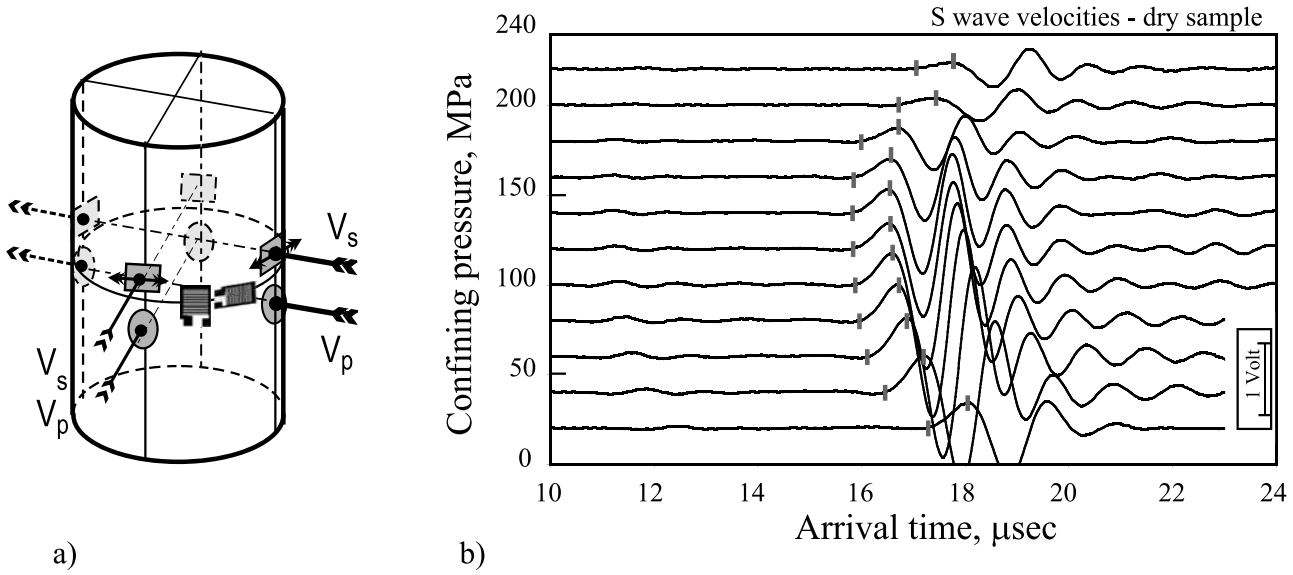

Figure 3. (a) Sample setup used in this study. The initial sample diameter and length were 40 mm and 80 mm, respectively. The velocities *P* and *S* were measured perpendicular to the main axis of the specimen. The PZT and strain gages were directly glued on the rock. (b) Example of received *S* waveforms at different confining pressures obtained in the dry experiment.

2.5. Experimental Procedure

[12] Two experiments, one in dry conditions, the other in wet conditions, were carried out under hydrostatic loading at a confining pressure up to 280 MPa. Inside the vessel, the sample was covered with a Neoprene jacket that insulated it from the confining oil.

[13] The dry sample was air dried at 50°C for 48 hours. The wet sample was immersed in tap water for 48 hours to ensure complete saturation before measurement. During the wet experiment, confining pressure was first increased to 5 MPa. Pore pressure and confining pressure were then raised up simultaneously to 1 and 6 MPa, respectively. Pressure was held constant for at least 12 hours to obtain full fluid saturation of the sample. At the beginning of the wet experiment, pore pressure and confining pressure were raised up to 10 and 20 MPa, respectively.

[14] During both experiments, confining pressure was varied in step of 5 MPa and the pressurization ramp was $\sim$0.05 MPa s^{-1}. At the end of each step, confining pressure was kept constant over a period of either 15 min ("during elastic compaction") or 60 minutes ("during cataclastic compaction"). These delays are required for two reasons: (1) they allow the changes in pore structure to stabilize during cataclastic compaction [*Zhang et al.*, 1990], and (2) as noted by *Gardner et al.* [1965] and *Christensen and Wang* [1985], there is a slow velocity drift, as the time for velocity stabilization is linked to the pore structure, the clay content, and the mineral contacts. Two examples of the evolution of the *P* wave velocity (wet experiment) versus time are given in Figure 4. In Figure 4a, when effective pressure is increased from 25 to 30 MPa (dashed curve), the velocity increases drastically by 25 m s^{-1} in 3 min and then increases slowly by less than 10 m s^{-1} in 10 min. After 15 min, the velocity is not totally stabilized, but its variations are small in comparison with the amplitude of the error bar (0.5%, which corresponds to 20 m s^{-1}). Figure 4b gives the evolution of the *P* wave velocities during the cataclastic compaction of the sample: When effective pressure is increased from 135 to 140 MPa (dashed curve), the velocity decreases. After 50 min, the velocity is stabilized, which allowed us to increase the effective pressure from 140 to 145 MPa after a step duration of 60 min.

[15] At the end of each experiment, the sample was carefully unloaded, decreasing confining pressure with 10 MPa decrements, and recovered for microstructural analysis.

3. Theoretical Background

3.1. General Relations for Elastic Energy of Cracked and Porous Rocks

[16] In porous rocks, changes in porosity alone are not sufficient to account quantitatively for the evolution of elastic properties. Because microcracks are very compliant, they have a major effect on elastic properties although they represent an extremely small amount of porosity, typically less than 1%. In porous rocks microcracks may be thought of as representatives of narrow gaps due to asperities in grain-to-grain contacts. Our choice of approximations (a model considering a mixture of spheroidal pores and penny-shaped cracks) results from a compromise between models simple enough to get closed forms for elastic moduli, and yet sophisticated enough to capture the key physical processes. Using *Kachanov* [1993] and *Shafiro and Kachanov* [1997], the effective elastic properties may be expressed in a unique manner as a function of the overall porosity p and the crack density ρ. The crack density is defined as $\rho = 1/V\sum^{N} c_i^3$, where c_i is the radius of the ith crack and N is the total number of cracks embedded in the representative elementary volume (REV) V. The elastic potential $f(\boldsymbol{\sigma})$ for a given tensor stress state

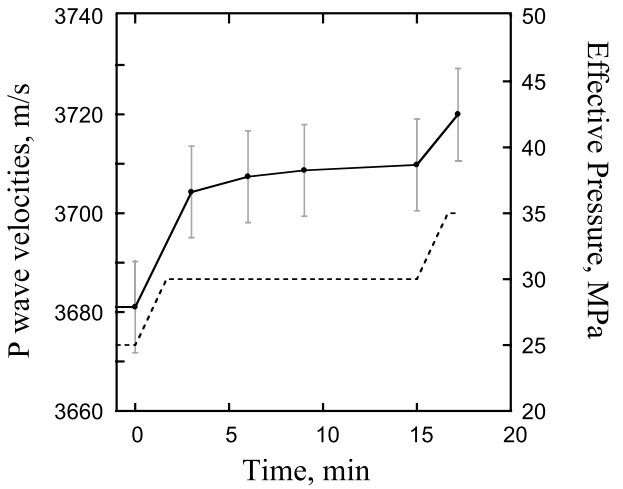

a) *Wet Sample (Time dependance of P-wave velocities during 'elastic compaction')*

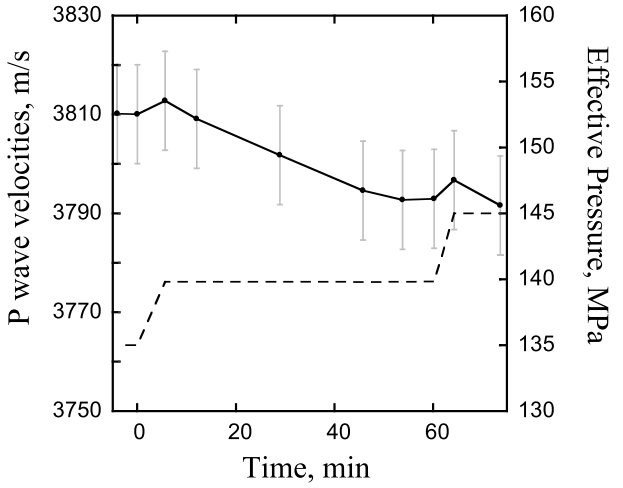

b) *Wet Sample (Time dependance of P-wave velocities during 'cataclastic compaction')*

Figure 4. Time dependence of P wave velocities. (a) Elastic compaction. When effective pressure is increased from 25 to 30 MPa (dashed curve), the velocity stabilized after 15 minutes. (b) Cataclastic compaction. When effective pressure is increased from 135 to 140 MPa (dashed curve), the velocity decreases; however, after 50 min, the velocity is stabilized, which allowed us to increase the effective pressure from 140 to 145 MPa after a step duration of 60 min.

$\boldsymbol{\sigma}$ (from which the macroscopic volume-averaged strains are obtained as $\varepsilon_{ij} = \partial f/\partial\sigma_{ij}$) may be written as a sum:

$$f = f_o + \Delta f, \tag{1}$$

where $f_o = 1/2E_o[(1 + \nu_o)\mathrm{tr}\,(\boldsymbol{\sigma}\cdot\boldsymbol{\sigma}) - \nu_o(\mathrm{tr}\,\boldsymbol{\sigma})^2]$ is the potential of the bulk material (E_o, ν_o are its Young's modulus and Poisson's ratio; $\mathrm{tr}\,(\boldsymbol{\sigma}\cdot\boldsymbol{\sigma}) = \sigma_{ij}\sigma_{ji}$ and $(\mathrm{tr}\,\boldsymbol{\sigma})^2 = (\sigma_{kk})^2$), and Δf is the additional term due to pores and cracks. The elastic potential Δf can be expressed as a sum [*Kachanov*, 1993]:

$$\Delta f = \frac{1}{\Gamma}\left(\Delta f_{\mathrm{nonint}}^{\mathrm{pores}} + \Delta f_{\mathrm{nonint}}^{\mathrm{cracks}}\right). \tag{2}$$

The second term in the parentheses is the potential associated to noninteracting cracks. In the crack case, as discussed by *Kachanov* [1993], *Sayers and Kachanov* [1995], and *Schubnel and Guéguen* [2003], the noninteraction scheme is valid up to crack density of at least 0.5. The first term in the parentheses is the potential associated to noninteracting pores. The effect of stress interactions between pores is taken into account in the term Γ. In the dry case, $\Gamma = 1 - p$ where p is the overall porosity [e.g., *Kachanov*, 1993]. This approach corresponds to Mori-Tanaka's model [*Mori and Tanaka*, 1973]. The interaction effect between cracks and pores is "asymmetric": cracks do no affect pores, whereas pores affect cracks. In the case where the rock is fluid saturated, the effect of stress interactions due to spheroidal pores can be neglected and $\Gamma = 1$.

[17] *Kachanov* [1993] gives the expression of the elastic potential associated with randomly oriented noninteracting cracks:

$$\Delta f_{\mathrm{nonint}}^{\mathrm{cracks}} = \rho\frac{h}{2E_o}\left\{\mathrm{tr}(\boldsymbol{\sigma}\cdot\boldsymbol{\sigma}) - \frac{1}{5}\left[1 - \left(1 - \frac{\nu_o}{2}\right)\frac{\delta}{1+\delta}\right] \times \left(2\,\mathrm{tr}(\boldsymbol{\sigma}\cdot\boldsymbol{\sigma}) + (\mathrm{tr}\,\boldsymbol{\sigma})^2\right)\right\}, \tag{3}$$

where h is a factor describing the penny-shaped geometry,

$$h = \frac{16(1-\nu_o^2)}{9(1-\nu_o/2)}. \tag{4}$$

Typically, $h \simeq 2$. The parameter δ characterizes the coupling between the solid stress and the fluid pressure, and thus determines the fluid impact on the effective crack compliance:

$$\delta = (1 - \nu_o/2)\frac{E_o\zeta}{K_f}h, \tag{5}$$

δ compares the fluid bulk modulus K_f to what is an apparent crack bulk modulus $(1 - \nu_o/2)E_o\zeta h$, where ζ is the crack aspect ratio, which is the ratio between the aperture to the diameter. In the dry case $\delta \to \infty$ [e.g., *Kachanov*, 1993; *Schubnel and Guéguen*, 2003].

[18] An expression of the elastic potential associated to noninteracting spheroidal pores is proposed by [*Shafiro and Kachanov*, 1997]

$$\Delta f_{\mathrm{nonint}}^{\mathrm{pores}} = p\frac{3(1-\nu_o)}{4E_o}\left\{\frac{10(1+\nu_o)}{7-5\nu_o}\mathrm{tr}(\boldsymbol{\sigma}\cdot\boldsymbol{\sigma}) - \left[\frac{1+5\nu_o}{7-5\nu_o} + \frac{1}{3(1+\delta_s)}\right](\mathrm{tr}\,\boldsymbol{\sigma})^2\right\}, \tag{6}$$

where δ_s incorporates the following physical parameters: the matrix stiffness, which is the stiffness of the solid portion,

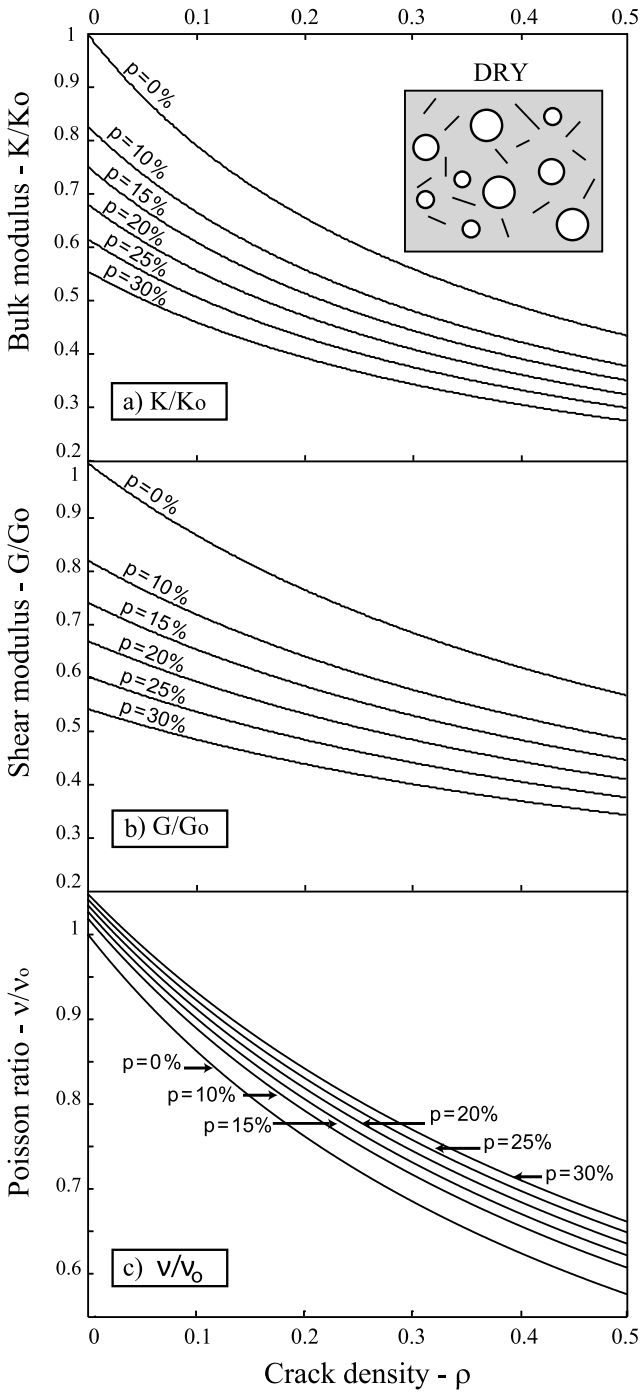

Figure 5. Effective elastic moduli of an idealized dry rock made of a mixture of penny-shaped cracks and spheroidal pores. (a) Effective bulk modulus K/K_o, (b) effective shear modulus G/G_o, and (c) effective Poisson ratio ν/ν_o plotted versus crack density ρ (range [0–0.5]). The curves are given at fixed porosity ϕ, which varies from $\phi = 0\%$ to $\phi = 30\%$. The bulk and shear moduli of the dry matrix (K_o, G_o) are summarized in Table 2.

the fluid compressibility, and the pore geometry. For a spherical pore, *Shafiro and Kachanov* [1997] showed that

$$\delta_s = \frac{2}{9}\frac{E_o/K_f - 3(1-2\nu_o)}{1-\nu_o}. \quad (7)$$

For liquid water ($K_f \simeq 2$ GPa) and elastic constants equal to $E_o = 40$ GPa and $\nu_o = 0.24$, δ_s is equal to 5.4.

3.2. Effective Moduli of Dry Rock

[19] In the dry case, the stress perturbations due to the presence of spheroidal pores is taken into account and $\Gamma = 1 - p$. Parameters δ and δ_s are very large. Thus, from equation (2), the effective shear modulus G (which can be directly inverted from the S wave velocities), and the effective bulk modulus K (which can be directly inverted from a combination of the P and S wave velocities), can be derived as

$$\frac{K_o}{K} = 1 + \frac{\rho}{1-p}\frac{h}{1-2\nu_o}\left\{1 - \frac{\nu_o}{2}\right\} + \frac{p}{1-p}\frac{3(1-\nu_o)}{2(1-2\nu_o)}, \quad (8)$$

$$\frac{G_o}{G} = 1 + \frac{\rho}{1-p}\frac{h}{1+\nu_o}\left\{1 - \frac{\nu_o}{5}\right\} + \frac{p}{1-p}\frac{15(1-\nu_o)}{7-5\nu_o}, \quad (9)$$

where K_o and G_o are the bulk and shear moduli of the crack- and porosity-free matrix. Note that a dry effective modulus is also called a dry frame modulus, it is also called the drained modulus in quasi-static poroelasticity theory. The evolution of the elastic moduli K/K_o, G/G_o, and ν/ν_o are plotted versus the crack density for different porosity values (range $\phi = 0$–30%) on Figures 5a, 5b, and 5c, respectively. Input data for the solid matrix are detailed in Table 2.

[20] The crack density being constant, a decrease in porosity induces a moderate increase of both the effective bulk and shear moduli while the Poisson ratio ν decreases slightly. Reciprocally, at a given porosity, an increase of the crack density reduces the bulk and shear moduli. However, the Poisson ratio (Figure 5c) is affected in a different manner by cracks and decreases with increasing crack density. Note that the effects of cracks and pores are opposite on ν/ν_o: An increase of crack density reduces ν/ν_o, whereas an increase of porosity increases ν/ν_o.

3.3. Effective Moduli of Fluid-Saturated Rock

[21] In the wet case, the bulk and shear moduli can also be derived from equation (2) and can be expressed as

$$\frac{K_o}{K} = 1 + \rho\frac{h}{1-2\nu_o}\left\{1 - \left[1 - \left(1 - \frac{\nu_o}{2}\right)\frac{\delta}{1+\delta}\right]\right\} + p\frac{3(1-\nu_o)}{2(1-2\nu_o)} \cdot \left\{1 - \frac{1}{1+\delta_s}\right\}, \quad (10)$$

$$\frac{G_o}{G} = 1 + \rho\frac{h}{1+\nu_o}\left\{1 - \frac{2}{5}\left[1 - \left(1 - \frac{\nu_o}{2}\right)\frac{\delta}{1+\delta}\right]\right\} + p\frac{15(1-\nu_o)}{7-5\nu_o}. \quad (11)$$

In this case, the bulk and shear moduli are functions of the elastic properties of the matrix, the porosity p, the crack

Table 2. Bulk Modulus K_o and Shear Modulus G_o of the Wet and Dry Matrix (Crack- and Porosity-Free)[a]

	Solid Matrix Dry	Solid Matrix Wet	Fluid
K_o, GPa	21.3	25.8	2
G_o, GPa	18	16.2	0

[a] K_o and G_o were calculated from the velocities data, assuming that the crack density $\rho = 0$ when the velocities reach maximum values during the experiments. Theses values are used in the effective medium model "cracks and pores."

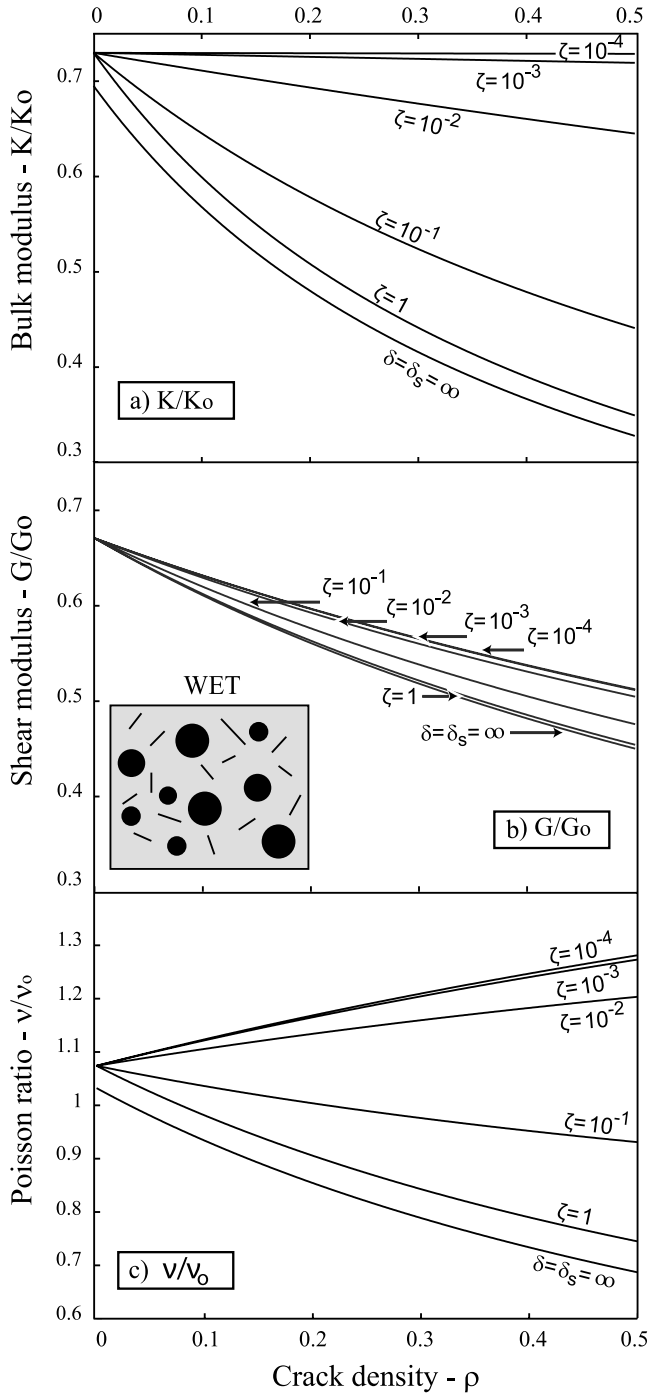

Figure 6. Effective elastic moduli of an idealized wet rock made of a mixture of penny-shaped cracks and spheroidal pores. (a) Effective bulk modulus K/K_o, (b) effective shear modulus G/G_o, and (c) effective Poisson ratio ν/ν_o plotted versus crack density ρ (range [0–0.5]). The curves are given at fixed aspect ratio ζ, which varies from $\zeta = 1$ to $\zeta = 10^{-4}$. In these plots the porosity is constant and $\phi = 20\%$. The bulk and shear moduli of the wet matrix (K_o, G_o) are summarized in Table 2.

density ρ, and the aspect ratio ζ (which affects the saturation parameter δ). As in the dry case, the bulk and shear moduli are inversely proportional to both the porosity and the crack density. A new important parameter to be taken into consideration here is the aspect ratio ζ. Figures 6a, 6b, and 6c show the evolution of both the bulk and shear moduli (K/K_o, G/G_o) and the Poisson's ratio ν/ν_o versus the crack density for different values of aspect ratio ζ. The porosity was fixed to 20%, and the matrix parameters are summarized in Table 2. For a fluid-saturated rock and an aspect ratio $\zeta < \sim 10^{-3}$ the bulk and shear moduli decrease as ρ increases. Note that the controlling parameters is δ. It is

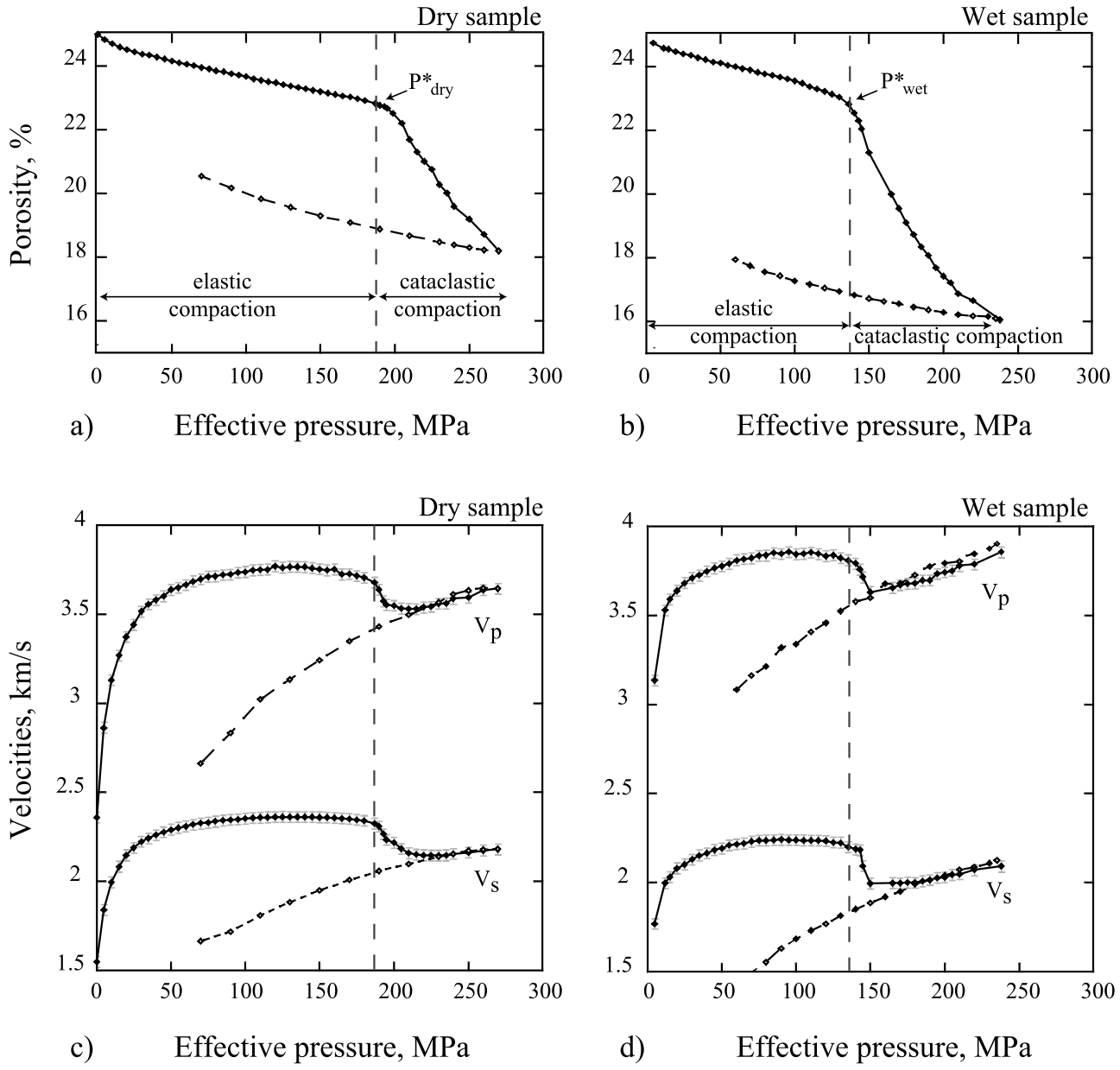

Figure 7. (a) and (b) Mechanical data for the dry and wet specimens. The porosity reduction is plotted versus effective pressure. The critical pressure P^* indicates the beginning of pore collapse and grain crushing. P^* is lower in the wet specimen than in the dry specimen, which is explained by chemical weakening effects. The unloading is plotted as dashed lines. (c) and (d) Velocity measurements for the dry and wet specimens. The elastic wave velocities P and S are plotted versus the effective pressure. At the critical pressure P^*, the velocities decrease because of grain crushing and pore collapse. Note that at pressure $P \simeq 220$ and $P \simeq 160$, in the dry and wet specimens, respectively, the velocities increase again. The unloading is plotted as dashed lines.

equivalent to increase δ by increasing ζ or decreasing K_f. The effect is the strongest (1) for the bulk modulus when compared to the shear modulus and (2) in the limiting cases $\zeta = 1$ (cracks are no longer cracks but spheres) or $\delta = \delta_s = \infty$ (dry medium). The evolution of Poisson's ratio ν/ν_o is very different compared to the dry case (Figure 6c): (1) if $10^{-1} < \zeta < 1$, ν/ν_o decreases slightly as ρ increases; and (2) however, if $10^{-4} < \zeta < 10^{-2}$, the Poisson's ratio increases as crack density increases. Such a behavior was also predicted by the differential self-consistent model of *Le Ravalec and Guéguen* [1996].

4. Results

4.1. Porosity Reduction Versus Pressure

[22] In the following, we use the convention that compressive stresses and compactive strains are positive. Pore pressure is denoted by P_p and the difference between

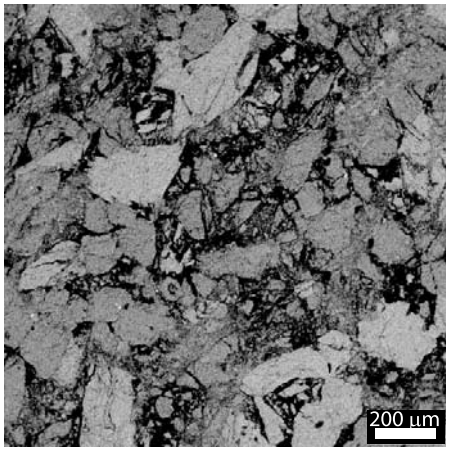

a)

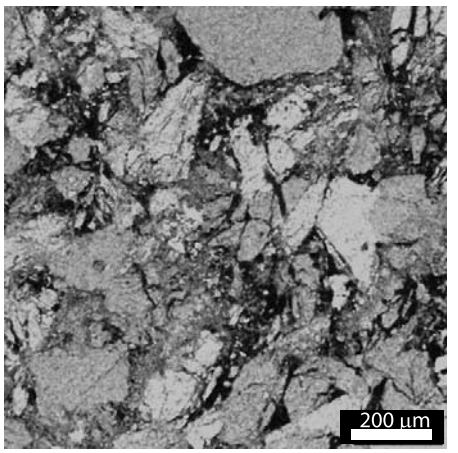

b)

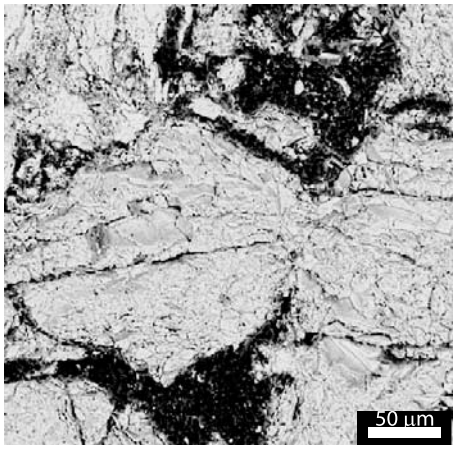

c)

Figure 8. SEM micrograph (backscattered) of Bleurswiller sandstone. Epoxy-filled pores appear in black. (a) and (b) Pictures of the specimens deformed under dry condition. Crushed grains and cement fragments fill pore space, which result in large decrease of the porosity. (c) Fractured grains at grain-grain contacts.

confining pressure P_c and pore pressure is referred to as "effective pressure" P.

[23] Figures 7a and 7b show the evolution of porosity versus effective pressure for the dry and wet experiments, respectively. In both cases, at $P < P^*$, porosity reduction shows a linear dependence with effective pressure. On both curves, the inflection point, P^*, corresponds to the onset of grain crushing and pore collapse [*Zhang et al.*, 1990; *Wong et al.*, 1997], equal to 180 and 135 MPa, in the dry and wet experiment, respectively. Beyond P^*, accelerating inelastic volume compaction occurs due to extensive grain crushing, grain displacement, and pore collapse. Although there are a number of common pressure-dependent features on the two plots, the water-saturated sample is much weaker than the dry one. Such a difference in stress/strain response is probably caused by chemical weakening effects and stress corrosion due to presence of a chemically active pore fluid and has already been observed in previous experiments [*Michalske and Freiman*, 1981; *Read et al.*, 1995; *Baud et al.*, 2000a]. Following *Baud et al.* [2000a], the water-weakening effect on grain crushing can be expressed as $P^*_{wet}/P^*_{dry} = (\gamma'/\gamma)^{3/2}$, where γ and γ' are the specific surface energies of the dry and wet matrices, respectively. Our experimental results yield to $\gamma'/\gamma = 0.82$, a value in the range of those observed in Darley Dale, Gosford, and Boise sandstones reported by *Baud et al.* [2000a].

4.2. Elastic Wave Velocities Data

[24] Figures 7c and 7d present the evolution of P and S wave velocities with effective pressure for the dry and wet experiment, respectively. A low effective pressure, up to 50 MPa, V_p and V_s increase drastically with pressure. Then for $50 < P < P^*$, the rate of increase in velocities is very small. Such a behavior in porous rocks has been reported by *Lo et al.* [1986]; *Ayling et al.* [1994]; *Prasad and Manghnani* [1997] and is interpreted by the closure of preexisting cracks and pores with small aspect ratios.

[25] However, at P^*, in dry or wet conditions and although porosity decreases, both P and S wave velocities drop sharply and decrease by several percent. This can only be explained by the nucleation and/or propagation of newly formed cracks appearing at high pressure. While pore collapse and porosity reduction tend to increase elastic wave velocities, newly formed cracks due to grain crushing tend to decrease the velocities. At first, increased damage and newly formed cracks play a dominant role. This result is consistent with the effective medium theory developed in section 3. Beyond P^*, Figures 7c and 7d show clear inflection points, at $P \simeq 220$ MPa and $P \simeq 160$ MPa in the dry and wet cases, respectively, where velocities start to increase again. At this point, the newly formed cracks are progressively being closed and the material becomes stiffer again.

[26] Velocities measured during depressurization (dashed lines on the plots) remain lower than those measured during pressurization, demonstrating the extensive damage accumulation as cracks reopen and propagate during unloading.

4.3. Microstructural Observations

[27] Detailed microstructural analysis was performed on the dry sample using scanning electron microscopy (SEM). To prepare SEM sections, samples 20×40 mm in size were cut parallel to the long specimen axis. Sections were

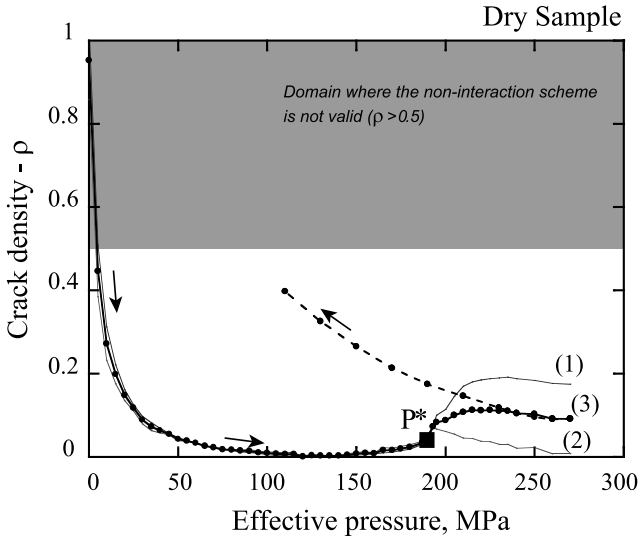

Figure 9. Evolution of crack density as a function of the effective pressure found in the dry specimen. Curves 1 and 2 show ρ values inverted from equation (9) (G modulus) and (8) (K modulus), respectively. Curve 3 shows the average between these two values of ρ. The beginning of pore collapse and grain crushing P^* is associated with an increase of the crack density. Curves 1 and 2 start to diverge at P^*, which may be explained by a mechanism of rolling contacts. The unloading is shown as a dashed line.

impregnated with epoxy and subsequently polished and gold coated.

[28] Thin sections do not reveal zones of localized crushing. Figures 8a and 8b are SEM micrographs of the deformed sample and illustrate the extensive grain crushing that took place during deformation (compare Figures 8a and 8b with Figure 1b). Grain fragments fill up the existing pores leading to a large decrease in the porosity. Crack nucleation takes place at grain-grain contacts (Figure 8c), resulting in cracks at a scale with the original grain size. Moreover the crushing of some grain produces small microcracks and the scale of the fine produced is of the order of few microns (Figures 8a and 8b). Note that after unloading the rock was still cohesive.

5. Interpretations

5.1. Crack Density Evolution as Inferred From Elastic Wave Velocities Variations

[29] The effective shear and bulk moduli G, K are directly inverted from elastic wave velocities data using

$$G = \psi V_s^2 \qquad \text{and} \qquad K = \psi\left(V_p^2 - \frac{4}{3}V_s^2\right).$$

[30] The bulk density of the rock ψ is corrected from porosity variations, with $\psi = \psi_o(1 - p)$ and $\psi_o = 2.6\ 10^3$ kg m^{-3}. We assume that the crack porosity variation is negligible compared to the overall porosity. When velocities reach maximum values: at $P \simeq 140$ MPa and $P \simeq 100$ MPa in the dry and wet experiment, respectively (Figure 7), the rock is considered to be crack free ($\rho = 0$) and the porosity is known. Then the shear and bulk moduli of the crack- and porosity-free matrix (K_oG_o) can be estimated. Those values are reported in Table 2.

5.1.1. Dry Experiment

[31] In the dry case, the effective medium model (pores and cracks) gives two independent relations (equations (8) and (9)) for a single crack parameter: the crack density. On Figure 9, the evolution of crack density is plotted versus pressure. Curve 1 plots ρ values inferred from S wave data (equation (9)) while curve 2 plots ρ values inferred from a combination of P and S waves data (equation (8)). Curve 3 plots the average of ρ obtained from those two values. Initially, crack density ρ decreases from 1 to 0 as the confining pressure P is raised from 0 to 50 MPa. Since the associated porosity reduction in this part of the loading path is small ($\sim$1%), the crack density decrease can be mainly attributed to viscoelastic closures of preexisting cracks and pores with small aspect ratio. Note that the agreement between the values inferred from equations (8) and (9) is excellent up to P^*.

[32] When pore collapse and grain crushing take place (at $P = P^*$), the crack density ρ raises from 0 to a mean value of 0.1 (curve 3). An anomalous feature just beyond P^* is that crack densities inferred from equations (8) and (9) become different: Inversion of G moduli gives a ρ value close to 0.2, whereas inversion of K moduli data gives a ρ value closer to 0.05. This discrepancy will be further analyzed in section 5.2. During depressurization (dashed lines), crack density increases drastically, showing not only crack reopening, but permanent damage accumulation.

5.1.2. Fluid-Saturated Experiment

[33] In the wet experiment, both crack density ρ and average aspect ratio ζ can be derived from the S and P wave data (equations (10) and (11)). Figure 10a plots crack density as a function of effective pressure. Figures 10a and 9 show some common features: a decrease of crack density from 1 to 0 in the first part of the loading path and then a jump at the beginning of pore collapse and grain crushing (at $P \geq P^*$). However, in this experiment, the crack density inferred beyond P^* is equal to $\rho = 0.4$, which is a much higher value than in the dry case. Such a difference could be explained by chemomechanical effects, in the same way P^* has a much lower value.

[34] The evolution of average crack aspect ratio with effective pressure P is given in Figure 10b. As effective pressure is raised from 0 to 60 MPa, average crack aspect ratio increase exponentially from 2×10^{-2} to 0.5. Indeed, as pressure increases, the thinnest, most compliant cracks are first closed and this process leads to an increase of the average crack aspect ratio. When 60 MPa $< P <$ 135 MPa, the crack density is fixed to 0, then from equations (10) and (11) there is an infinite number of solutions for ζ. However, we can imagine that during this stage, all compliant cracks are closed, which leads, in theory, to an average aspect ratio close to 1. At P^*, the average aspect ratio decreases suddenly from 0.5 to $\zeta = 3 \times 10^{-3}$, showing that new cracks were created at that point. Then beyond P^*, ζ decreases exponentially to reach a final value of 3×10^{-4} at 250 MPa. At the end of this experiment, the average crack aspect ratio is much lower than at the beginning (more than one order of magnitude).

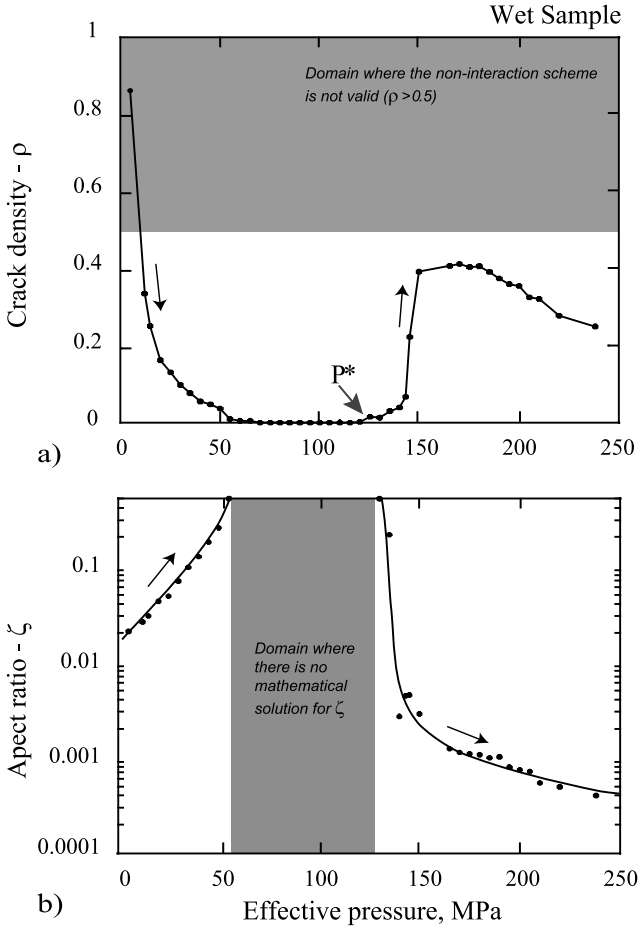

Figure 10. (a) Evolution of crack density and (b) aspect ratio as functions of the effective pressure in the wet specimen. P^* is associated with an increase of crack density higher than these found in Figure 8. The cracks created at the beginning of grain crushing ($P > P^*$) have small aspect ratio, $\zeta < 10^{-2}$.

This implies that the mechanism of grain crushing create very thin cracks, which in agreement with our postmortem microstructural observations.

[35] These simple inversion results show that our effective medium model is a very powerful tool in order to describe the physical state of damage within a saturated rock.

5.2. Evolution of the Ratios V_p/V_s

[36] Taking into consideration V_p/V_s ratio leads to look at the rock from two different and complementary point of views.

5.2.1. Effective Medium Model

[37] Figure 11 plots the evolution of V_p/V_s ratios in the dry and wet experiments. On Figure 11, dots correspond to the experimental data, and solid lines represent the estimated values of V_p/V_s as inferred from the effective medium model, using the values for mean crack densities and aspect ratio shown on Figures 9 and 10. Recalling that V_p/V_s is a single function of Poisson ratio ($(V_p/V_s)^2 = 2(1 - \nu)/1 - 2\nu$), an increase in V_p/V_s is associated with an increase in ν and reciprocally. In the dry case, the V_p/V_s ratio of dry rock increases substantially with increasing pressure (for $P <$ 50 MPa). Again, this is a consequence of the viscoelastic closure of the preexisting cracks. In contrast, in the same range of pressure, when the rock is saturated with water, the V_p/V_s ratio decreases as effective pressure increases. Similar observations have been reported in previous experiments [*Nur and Wang*, 1989; *Dvorkin and Walls*, 2000]. In this pressure range, both in the dry and wet cases, the agreement between experimental data and predicted value from EM theory is good. Between 50 MPa and P^*, the V_p/V_s ratio is a constant which reflects the intrinsic rock properties: V_p/V_s = 1.59 and V_p/V_s = 1.72 in the dry and wet case, respectively. V_p/V_s is larger in saturated conditions, which is in agreement with the result of Gassmann's static theory [*Gassmann*, 1951] and previous experimental studies [*Nur and Wang*, 1989].

[38] Our experimental observations show that cataclastic compaction is associated with a sudden increase of the V_p/V_s ratio ($P \geq P^*$), this is observed both in wet and dry conditions (Figure 11). This increase in V_p/V_s ratio is only well predicted by the effective medium model in wet condition. This is explained by the additional crack parameter ζ used in model, and the dominant effect of average crack aspect ratio reduction (ζ is in the range 10^{-2}–10^{-4} at $P > P^*$, see Figures 10b and 6c) during closure of the newly formed cracks.

[39] In the dry case, however, our modeling does not predict an increase of the V_p/V_s ratio with increasing crack density but rather a slight decrease (Figures 11 and 5c). This last observation points out the limit of the previous effective medium model, which seems to be a better approximation in saturated conditions than in dry ones. This is probably due to the fact that stress interactions between cracks are larger in dry than saturated conditions, as water tends to act as a screen to stress perturbations. Thus the noninteraction approximation is likely to be a better approximation in

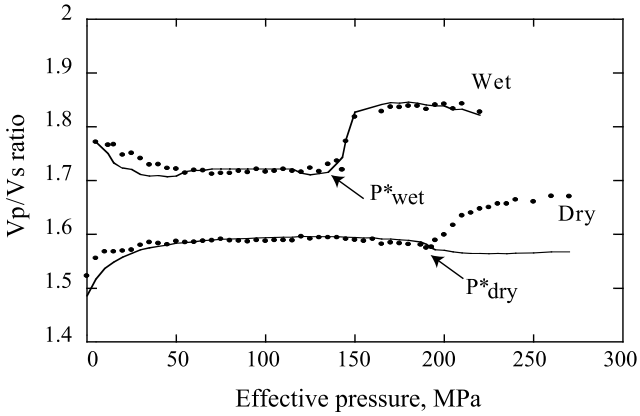

Figure 11. Evolution of the V_p/V_s ratio in the wet and dry specimens as functions of effective pressure. Dots are experimental data. The curves are estimations of V_p/V_s derived from the effective medium model "cracks and pores," using crack density and aspect ratio shown in Figures 9 and 10. When pore collapse and grain crushing occur in the dry specimen, experimental data show an increase of V_p/V_s, which is not predicted by the effective medium model (see Figure 5c).

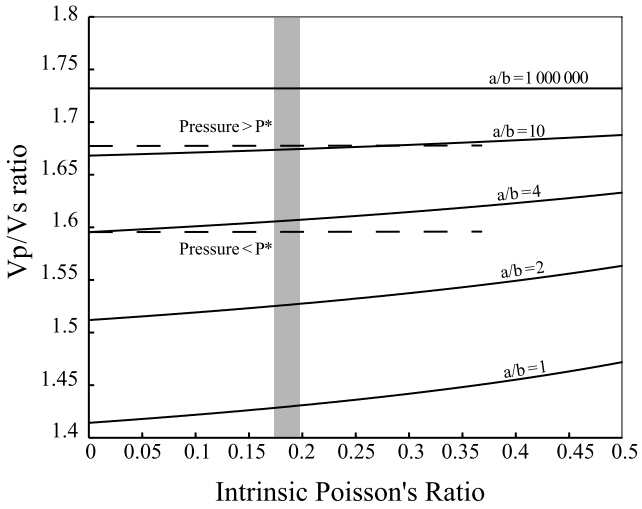

Figure 12. Digby's model. It is a granular model introducing b = bonding radius and a = contact radius. It gives the evolution of the ratio V_p/V_s as a function of the intrinsic Poisson's ratio of the grain, for different value of a/b. When $P < P^*$, $V_p/V_s = 1.59$, which corresponds to $a/b \simeq 3.5$, with an intrinsic Poisson ratio fixed at $\nu_o = 0.18$, when $P > P^*$, $V_p/V_s = 1.67$, and $a/b \simeq 12$. The physical explanation is that most grains are no more bonded at this second stage, which yields to lower values of b.

wet conditions. Additionally, and most importantly, the extra crack parameter ζ, which is absent in the dry scheme, enables a finer description of the rock microstructural evolution, and increases the degree of freedom in the elastic wave velocity inversion from -1 to zero.

5.2.2. Granular Model

[40] An alternative approach can be followed in order to understand the evolution of the V_p/V_s ratio in dry conditions. While the previous effective medium model considers the rock as a continuous matrix containing inclusions (here pores and cracks), a complementary view is to look at it as a discontinuous granular medium. In such way, *Digby*'s [1981] dry granular medium model assumes that the rock is a homogeneous and isotropic granular medium, formed by randomly packed spherical grains. Neighboring spheres of radius R are initially firmly bonded across small, circular regions of average radius b. As the hydrostatic pressure increases in the medium, the spheres deform in such a way that the contact regions of all the neighboring spheres increases up to a radius a but remain flat and circular. In such a configuration, $a \geq b$ and $a, b \ll R$. The simple case $b = a$ corresponds to the usual Hertz-Mindlin result where the contact is infinitely rough and no slip is allowed. On the contrary, for an unconsolidated sand, b goes to zero. Using *Digby's* [1981] model, the V_p/V_s ratio can be expressed as

$$\left(\frac{V_p}{V_s}\right)^2 = \frac{3\frac{a}{b}(2-\nu_o)+4(1-\nu_o)}{\frac{a}{b}(2-\nu_o)+3(1-\nu_o)}, \qquad (12)$$

where ν_o is the Poisson ratio of the solid grains. The V_p/V_s ratio is now again a function of two independent dimensionless quantities: (a/b) and ν_o. The evolution of the V_p/V_s ratio is plotted as function of ν_o for different values of a/b on Figure 12. Note that the V_p/V_s ratio depends weakly on initial ν_o value. Figure 12 shows that the important parameter here is (a/b). *Digby*'s [1981] model predicts a maximum value of $V_p/V_s \simeq 1.74$ when $b \to 0$.

[41] In dry conditions and in the range 50 MPa $< P < P^*$, $V_p/V_s = 1.59$. Using equation (12) and $\nu_o \sim 0.18$ yields $a/b \simeq 3.5$. At $P > 220$ MPa, $V_p/V_s = 1.67$ is consistent with $a/b \simeq 12$. Such an increase in (a/b) beyond P^* can be interpreted as a decrease in b, the bonding radius, which means the grains are less cemented. This is exactly what is expected from grain crushing, as it produces small uncemented grains (Figure 8). However, because only a fraction of the original grains have been crushed at the end of our experiments (the rock is still cohesive when retrieved from the pressure vessel), the maximum value of $V_p/V_s = 1.74$ is not reached. The above interpretation allows us to add some complementary comments to section 5.1.1. As pointed previously, Figure 9 shows that the dry crack density inverted from shear waves alone is larger than the one inverted from both compressional and shear waves. This, in fact, implies that the shear modulus G "sees" more damage than the bulk modulus K and suggests that the new grains contacts of the small uncemented grains produced by crushing resist better to compression than to shear, just as rolling contacts do.

5.3. Comparison With Other Studies Done on Sandstones and Limestones

[42] Only few studies report the simultaneous evolutions of elastic wave velocities and porosity during pore collapse and grain crushing in porous rocks. *Johnston and Toksöz* [1980] and *Nur and Simmons* [1969] report experimental results obtained on Bedford limestone, a coarse-grained biogenetic limestone, poorly cemented by crystalline calcite with an initial porosity of 12%. Their experiments were performed in dry conditions and porosity reduction was calculated from axial strain measurements only, assuming that the deformation in the rock was isotropic. Figure 13 summarizes their results: Porosity reduction (Figure 13a), P wave velocities (Figure 13b), and S wave velocities (Figure 13c) are plotted versus effective pressure. The onset of pore collapse was reached at $P^* \sim 100$ MPa (Figure 13a). In contrast to Bleurswiller sandstone, the P and S wave velocities both increased as P^* was reached. Again and as discussed throughout our study, the balance between the effects of an increase in crack density and a reduction of porosity can be invoked to explain the decoupling between the evolution of elastic wave velocities and porosity. In contrast with our experimental results obtained on a higher porosity rock, porosity reduction seemed to have a dominant effect on the evolution of elastic wave velocities. However, this would not longer be true if the rock's initial porosity was smaller, such as in the case of Solnhoffen limestone ($p \sim 4\%$), as reported recently by *Schubnel et al.* [2005]. Therefore there must be a critical porosity under which the effect of porosity reduction becomes dominant during pore collapse. In sandstones, this critical porosity is high (>25%), whereas in limestones, it seems to be in between 4 and 12%. Such a difference between limestones and sandstones can be explained by the micromechanisms associated with pore collapse itself. In sandstones, pore

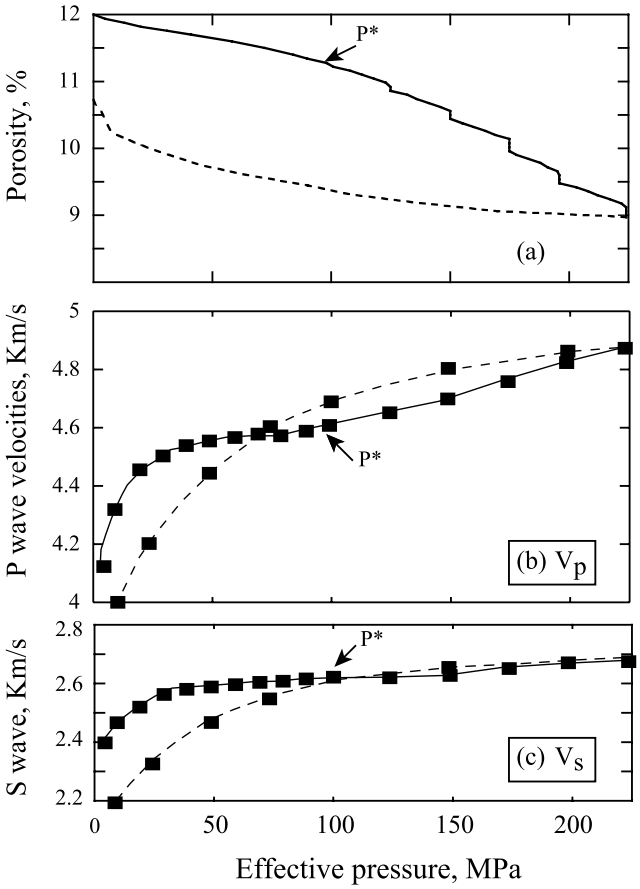

Figure 13. Dry hydrostatic compaction of Bedford limestone [from *Johnston and Toksöz*, 1980]. (a) Porosity reduction, (b) *P* wave velocities, and (c) *S* wave velocities as a function of effective pressure. In contrast with the experiments performed on Bleurswiller sandstone, the beginning of pore collapse (*P**) is associated with an increase of the *P* and *S* wave velocities. The behavior of the velocities is explained by the micromechanisms of the deformation: In limestone, pore collapse is mainly due to calcite plasticity, and grain crushing is minor. Dashed lines represent unloading.

collapse is a result of grain crushing [*Zhang et al.*, 1990; *Ménendez et al.*, 1996] as porosity reduction is the consequence of the filling of pore space by fragmented grains. In limestones, however, pore collapse is the result of intragranular plasticity of calcite, i.e., twinning and dislocation glide [*Fredrich et al.*, 1989; *Baud et al.*, 2000b; *Vajdova et al.*, 2004; *Schubnel et al.*, 2005]. Hence cracking might be less pervasive and crack densities likely smaller. Nevertheless, the evolution of dynamic elastic properties during the deformation of limestones could probably be predicted successfully using the effective medium model pores and cracks that we presented in this study (see Figures 5 and 6).

[43] Finally, we would like to point out that both in limestones and sandstones, depressurization induces large decreases of elastic wave velocities (dashed lines on Figure 13), which proves the important role played by stress relief cracking in crack propagation. Such an observation was also performed on very low porosity calcic rocks such as Carrara marble and Solnhoffen limestone [*Schubnel et al.*, 2005] and even granites from the URL underground laboratory [*Collins and Young*, 2000]. This points out as well the limitations of postmortem microstructural investigations.

6. Conclusions

[44] Elastic *P* and *S* wave velocities have been measured during hydrostatic compression of the Bleurswiller sandstone in both dry and wet conditions. During the first part of the loading, the elastic wave velocities increased due to the closure of preexisting cracks, then the rate of increase in velocities was very small. Beyond a critical effective pressure *P**, pore collapse and grain crushing took place, which was readily confirmed by microstructural observations. However, and counter intuitively, both *P* and *S* wave velocities decrease at *P**. This could nevertheless be interpreted by showing that newly formed cracks produced by grain crushing played a dominant role on the evolution of elastic wave velocities.

[45] A new effective medium model [*Kachanov*, 1993; *Shafiro and Kachanov*, 1997] containing both penny shaped cracks and spheroidal holes, enabled us to interpret our experimental results in terms of the competition arising from an increase in crack density and a decrease of porosity during grain crushing and pore collapse. This model was proven to be a very powerful tool in order to quantify the physical state of the crack population within a rock. In particular, the model permitted retracing the evolution of both the crack density and the average aspect ratio from elastic wave velocities, and thus quantification of viscoelastic crack closure/opening, damage accumulation, and/or crack propagation during an entire loading cycle. Similar inversions were performed recently in nonporous rocks with equal success [*Benson et al.*, 2006; *Schubnel et al.*, 2006]. However, the model seems to be more reliable in wet conditions. In dry conditions, the model failed in predicting the observed increase of the V_p/V_s ratio during pore collapse and grain crushing. An alternative approach was then used, based on *Digby*'s [1981] granular media modeling. It showed that the increase in V_p/V_s ratio can be analyzed as a transformation of the rock into a granular uncemented medium.

[46] The ratio V_p/V_s is a quantity frequently used in seismology and V_p/V_s anomalies have sometimes been recorded before and after earthquakes. For example, after the Antofagasta earthquake, an anomaly of V_p/V_s was observed [*Husen and Kissling*, 2001; *Koerner et al.*, 2004]: V_p/V_s increased from 1.72 to a significant mean value of 1.77. *Husen and Kissling* [2001] suggested that the anomaly was fluid driven. Indeed, an increase of V_p/V_s at low temperature is, in general, interpreted in terms of fluid content for the sole reason that elastic wave velocities are dramatically affected by pore fluid properties. Compressional wave velocities are higher in fluid saturated rocks than in dry rocks, whereas the shear velocities are about the same which results in an overall increase of the V_p/V_s ratio [*Gassmann*, 1951]. However, the experimental results reported in this study show that grain crushing can induce an increase in V_p/V_s as well. In our case, the V_p/V_s ratio increased from 1.59 to 1.67 in the dry case, and from 1.72 to

>1.8 in the wet case (note that the analogy between field and experimental data is strictly valid for the dry case, for the wet case frequency effect due to high frequency used in the laboratory should be corrected). This result has been interpreted in the wet case as the result of both damage accumulation (increase in crack density) and crack geometry (newly formed cracks with low aspect ratio $<10^{-2}$). In the dry case, grains are becoming less and less cemented so that the rock is losing its cohesion. The physical implication is that V_p/V_s is not only a function of the saturation, but also of the microstructural state of the rock, i.e., of the crack density, the average crack aspect ratio, and the overall cohesion of the grains. This might have important implications for the understanding of V_p/V_s anomalies in fault zones and fault gouges in the field.

[47] **Acknowledgments.** The technical skills of Guy Marolleau and Thierry Descamps have proved to be of major assistance, and both of them are greatly acknowledged. This work also benefited from discussion with many scientists. Among them, the authors would like to thank particularly Sergei Stanchits and Georg Dresen. The third author was supported by the Lassonde Institute, Toronto. Partial financial support for this work was provided by the CNRS.

References

Avseth, P., J. Dvorkin, G. Mavko, and J. Rykkje (1998), Diagnosing high-porosity sandstones for reservoir characterization using sonic and seismic data, paper presented at SEG Annual Convention, New Orleans, La., Sept.

Ayling, M. R., P. G. Meredith, and S. Murrell (1994), Microcracking during triaxial deformation of porous rocks monitored by changes in rock physical properties, I. Elastic-wave propagation measurements on dry rocks, *Tectonophysics*, *245*, 205–221.

Baud, P., W. Zhu, and T.-F. Wong (2000a), Failure mode and weakening effect of water sandstone, *J. Geophys. Res.*, *105*, 16,371–19,390.

Baud, P., A. Schubnel, and T.-F. Wong (2000b), Dilatancy, compaction and failure mode in Solnhofen limestone, *J. Geophys. Res.*, *105*, 19,289–19,320.

Baud, P., E. Klein, and T.-F. Wong (2004), Compaction localization in porous sandstones: Spatial evolution of damage and acoustic emission activity, *J. Struct. Geol.*, *26*, 603–624.

Benson, P., A. Schubnel, S. Vinciguerra, C. Trovato, P. Meredith, and R. P. Young (2006), Modeling the permeability evolution of microcracked rocks from elastic wave velocity inversion at elevated isostatic pressure, *J. Geophys. Res.*, *111*, B04202, doi:10.1029/2005JB003710.

Bristow, J. R. (1960), Microcracks and the static and dynamic elastic constants of annealed and heavily cold-worked metals, *Br. J. Apple. Phys.*, *11*, 81–85.

Christensen, N. I., and H. F. Wang (1985), The influence of pore pressure and confining pressure on dynamic elastic properties of Berea sandstone, *Geophysics*, *50*, 207–213.

Collins, D. S., and R. P. Young (2000), Lithological controls on seismicity in granitic rocks, *Bull. Seismol. Soc. Am.*, *90*, 709–723.

Digby, P. J. (1981), The effective elastic moduli of porous rocks, *J. Appl. Mech.*, *48*, 803–808.

Dvorkin, J., and A. Nur (1996), Elasticity of high-porosity sandstones: Theory for two North Sea datasets, *Geophysics*, *61*, 1363–1370.

Dvorkin, J., and J. Walls (2000), Detecting overpressure from seismic velocity calibrated to log and core measurements, *Annu. Offshore Technol. Conf. OTC 11912*, *32*, 11 pp.

Fortin, J., A. Schubnel, and Y. Guéguen (2005), Elastic wave velocities and permeability evolution during compaction of Bleurswiller sandstone, *Int. J. Rock. Mech. Min. Sci. Geomech.*, *25*, 873–889.

Fortin, J., S. Stanchits, G. Dresen, and Y. Guguen (2006), Acoustic emission and velocities associated with the formation of compaction bands in sandstone, *J. Geophys. Res.*, *111*, B10203, doi:10.1029/2005JB003854.

Fredrich, J. T., B. Evans, and T.-F. Wong (1989), Micromechanics of the brittle to plastic transition in Carrara marble, *J. Geophys. Res.*, *94*, 4129–4145.

Fredrich, J. T., G. L. Deitrick, J. G. Arguello, and E. P. de Rouffignac (1998), Reservoir compaction, surface subsidence, and casing damage: A geomechanics approach to mitigation and reservoir management, in *Eurorock-Rock Mechanics in Petroleum Engineering*, *SPE/ISRM 47284*, 403–412, Soc. of Pet. Eng., Inc., Richardson, Tex.

Gardner, G. H. F., M. R. J. Wyllie, and D. M. Droschak (1965), Hysteresis in the velocity-pressure characteristics of rocks, *Geophysics*, *30*, 111–116.

Gassmann, F. (1951), Elasticity of high-porosity sandstone: Uber die elastizitat poroser medien, *Vierteljahrsschr. Nat. Ges. Zurich*, *96*, 1–23.

Giles, M. R. (1997), *Diagenesis and Its Impact on Rock Properties: A Quantitative Perspective*, 520 pp., Kluwer Acad., Hingham, Mass.

Hadley, K. (1976), Comparison of calculated and observed crack densities and seismic velocities in Westerly granite, *J. Geophys. Res.*, *81*, 3484–3493.

Hashin, Z. (1988), The differential scheme and its application to cracked materials, *J. Mech. Phys. Solids*, *36*, 719–734.

Husen, S., and E. Kissling (2001), Postseismic fluid flow after the large subduction earthquake of Antofagasta, Chile, *Geology*, *29*, 847–850.

Johnston, D. H., and N. Toksöz (1980), Ultrasonic *P* and *S* wave attenuation in dry and saturated rocks under pressure, *J. Geophys. Res.*, *85*, 925–936.

Kachanov, M. (1980), Continuum model of medium with cracks, *J. Eng. Mech. Div.*, *106*, 1039–1051.

Kachanov, M. (1993), Elastic solids with many cracks and related problems, *Adv. Appl. Mech.*, *30*, 259–445.

Kachanov, M., I. Tsukrov, and B. Shafiro (1994), Effective moduli of solids with cavities of various shapes, *Appl. Mech. Rev.*, *47*, S151–S174.

Karner, S. L., F. M. Chester, A. K. Kronenberg, and J. S. Chester (2003), Subcritical compaction and yielding of granular quartz sand, *Tectonophysics*, *377*, 357–381.

Klein, E., P. Baud, T. Reuschle, and T.-F. Wong (2001), Mechanical behaviour and failure mode of Bentheim sandstone under triaxial compression, *Phys. Chem. Earth, Part A*, *26*, 21–25.

Koerner, A., E. Kissling, and S. A. Miller (2004), A model of deep crustal fluid flow following the M_w = 8.0 Antofagasta, Chile, earthquake, *J. Geophys. Res.*, *109*, B06307, doi:10.1029/2003JB002816.

Lehner, F., and Y. Leroy (2004), Sandstone compaction by intergranular pressure solution, in *Mechanics of Fluid- Saturated Rocks*, *Int. Geophys. Ser.*, vol. 89, edited by Y. Guéguen, and M. Bouteca, pp. 115–168, Elsevier, New York.

Le Ravalec, M., and Y. Guéguen (1996), High- and low- frequency elastic moduli for a saturated porous/cracked rock-Differential self-consistent and poroelastic theories, *Geophysics*, *61*, 1080–1094.

Lo, T.-W., K. B. Coyner, and M. N. Toksöz (1986), Experimental determination of elastic anisotropy of Berea sandstone, Chicopee shale, and Chelmsford granite, *Geophysics*, *51*, 164–171.

Ménendez, B., W. Zhu, and T.-F. Wong (1996), Micromechanics of brittle faulting and cataclastic flow in Berea sandstone, *J. Struct. Geol.*, *18*, 1–16.

Michalske, T. A., and S. W. Freiman (1981), A molecular interpretation of stress corrosion in silica, *Nature*, *295*, 511–512.

Mollema, P. N., and M. A. Antonellini (1996), Compaction bands: A structural analog for anti-mode I crack in aeolian sandstone, *Tectonophysics*, *267*, 209–228.

Mori, T., and K. Tanaka (1973), Average stress in matrix and average elastic energy of materials with misfitting inclusions, *Acta Meteorol.*, *21*, 571–574.

Nur, A., and G. Simmons (1969), The effect of saturation on velocity in low porosity rocks, *Earth Planet. Sci. Lett.*, *7*, 183–193.

Nur, A., and Z. Wang (1989), *Seismic and Acoustic Velocities in Reservoir Rocks*, vol. 1, *Experimental Studies*, *Geophys. Reprint Ser.*, vol. 10, Soc. of Explor. Geophys.s, Tulsa, Okla.

O'Connell, R., and B. Budiansky (1974), Seismic velocities in dry and saturated rocks, *J. Geophys. Res.*, *79*, 5412–5426.

O'Connell, R., and B. Budiansky (1977), Viscoelastic properties of fluid saturated cracked solids, *J. Geophys. Res.*, *82*, 5719–5736.

Olsson, W. A. (1999), Theoretical and experimental investigation of compaction bands in porous rock, *J. Geophys. Res.*, *104*, 7219–7228.

Prasad, M., and M. H. Manghnani (1997), Effects of pore and differential pressure on compressional wave velocity and quality factor in Berea and Michigan sandstones, *Geophysics*, *62*, 1163–1176.

Ramm, M. (1992), Porosity-depth trends in reservoir sandstones: offshore Norway, *Mar. Pet. Geol.*, *9*, 553–567.

Read, M. D., M. R. Ayling, P. G. Meredith, and S. Murrell (1995), Microcracking during triaxial deformation of porous rocks monitored by changes in rock physical properties, II. Pore volumometry and acoustic emission measurements on water-saturated rocks, *Tectonophysics*, *245*, 223–235.

Rudnicki, J. W. (2004), Shear and compaction band formation on an elliptic yield cap, *J. Geophys. Res.*, *109*, B03402, doi:10.1029/2003JB002633.

Salganik, R. L. (1973), Mechanics of bodies with many cracks, *Mech. Solids*, *8*, 135–143.

Sayers, C. M., and M. Kachanov (1995), Microcracks induced elastic wave anisotropy of brittle rocks, *J. Geophys. Res.*, *100*, 4149–4156.

Schubnel, A., and Y. Guéguen (2003), Dispersion and anisotropy of elastic waves in cracked rocks, *J. Geophys. Res.*, *108*(B2), 2101, doi:10.1029/2002JB001824.

Schubnel, A., J. Fortin, L. Burlini, and Y. Guéguen (2005), Damage and elastic recovery of calcite-rich rocks deformed in the cataclastic regime, *J. Geol. Soc. London, Special Edition on High Strain*, 203–221.

Schubnel, A., P. Benson, B. Thompson, J. Hazzard, and R. P. Young (2006), Quantify damage, saturation and anisotropy in cracked rocks by inverting elastic wave velocities, *Pure Appl. Geophys.*, *163*, 947–973, doi:10.1007/s00024-006-0061-y.

Scott, T. E., Q. Ma, and T. C. Roegiers (1993), Acoustic velocity changes during shear enhanced compaction of sandstone, *Int. J. Rock Mech. Min. Sci. Geomech.*, *30*, 763–769.

Shafiro, B., and M. Kachanov (1997), Materials with fluid-filled pores of various shapes: Effective elastic properties and fluid pressure polarization, *Int. J. Solids Struct.*, *34*, 3517–3540.

Shapiro, S. (2003), Piezosensitivity of porous and fractured rocks, *Geophysics*, *68*, 482–486.

Smits, R. M. M., J. A. de Wall, and J. F. C. van Kooten (1988), Prediction of abrupt reservoir compaction and subsurface subsidence by pore collapse in carbonates, *SPE Form. Eval.*, *3*, 340–346.

Vajdova, V., P. Baud, and T. Wong (2004), Compaction, dilatancy, and failure in porous carbonate rocks, *J. Geophys. Res.*, *109*, B05204, doi:10.1029/2003JB002508.

Walsh, J. B. (1965), The effect of cracks on the compressibility of rocks, *J. Geophys. Res.*, *70*, 381–389.

Wong, T.-F., C. David, and W. Zhu (1997), The transition from brittle faulting to cataclastic flow in porous sandstone: Mechanical deformation, *J. Geophys. Res.*, *102*, 3009–3026.

Wong, T.-F., C. David, and B. Menéndez (2004), Mechanical compaction, in *Mechanics of Fluid-Saturated Rocks*, *Int. Geophys. Ser.*, vol. 89, edited by Y. Guéguen and M. Bouteca, pp. 55–114, Elsevier, New York.

Zhang, J., T.-F. Wong, and D. M. Davis (1990), Micromechanics of pressure-induced grain crushing in porous rocks, *J. Geophys. Res.*, *95*, 341–352.

Zimmerman, R., W. Somerton, and M. King (1986), Compressibility of porous rocks, *J. Geophys. Res.*, *91*, 12,765–12,777.

J. Fortin and Y. Guéguen, Laboratoire de Géologie, Ecole Normale Supérieure, 24 rue Lhomond, F-75005 Paris, France. (fortin@geologie.ens.fr)

A. Schubnel, Lassonde Institute, University of Toronto, 170 College Street, Toronto, ON, Canada M5S 3E3.